

High-throughput ptychography using Eiger: scanning X-ray nano-imaging of extended regions

Manuel Guizar-Sicairos,* Ian Johnson, Ana Diaz, Mirko Holler, Petri Karvinen, Hans-Christian Stadler, Roberto Dinapoli, Oliver Bunk, and Andreas Menzel

Swiss Light Source, Paul Scherrer Institut, 5232 Villigen PSI, Switzerland

[*manuel.guizar-sicairos@psi.ch](mailto:manuel.guizar-sicairos@psi.ch)

Abstract: The smaller pixel size and high frame rate of next-generation photon counting pixel detectors opens new opportunities for the application of X-ray coherent diffractive imaging (CDI). In this manuscript we demonstrate fast image acquisition for ptychography using an Eiger detector. We achieve above 25,000 resolution elements per second, or an effective dwell time of 40 μ s per resolution element, when imaging a $500\text{ }\mu\text{m} \times 290\text{ }\mu\text{m}$ region of an integrated electronic circuit with 41 nm resolution. We further present the application of a scheme of sharing information between image parts that allows the field of view to exceed the range of the piezoelectric scanning system and requirements on the stability of the illumination to be relaxed.

© 2014 Optical Society of America

OCIS codes: (100.5070) Phase retrieval; (040.7480) Detectors, x-rays, soft x-rays, extreme ultraviolet (EUV); (100.3010) Image reconstruction techniques; (180.7460) X-ray microscopy.

References and links

1. J. Miao, P. Charalambous, J. Kirz, and D. Sayre, "Extending the methodology of X-ray crystallography to allow imaging of micrometre-sized non-crystalline specimens," *Nature* **400**, 342–344 (1999).
2. R. W. Gerchberg, "A practical algorithm for the determination of phase from image and diffraction plane pictures," *Optik* **35**, 237 (1972).
3. J. R. Fienup, "Phase retrieval algorithms: a comparison," *Appl. Opt.* **21**, 2758–2769 (1982).
4. B. Abbey, K. Nugent, G. Williams, J. Clark, A. Peele, M. Pfeiffer, M. de Jonge, and I. McNulty, "Keyhole coherent diffractive imaging," *Nat. Phys.* **4**, 394–398 (2008).
5. H. M. L. Faulkner and J. M. Rodenburg, "Movable aperture lensless transmission microscopy: A novel phase retrieval algorithm," *Phys. Rev. Lett.* **93**, 023903 (2004).
6. M. Guizar-Sicairos and J. R. Fienup, "Phase retrieval with transverse translation diversity: a nonlinear optimization approach," *Opt. Express* **16**, 7264–7278 (2008).
7. P. Thibault, M. Dierolf, A. Menzel, O. Bunk, C. David, and F. Pfeiffer, "High-resolution scanning X-ray diffraction microscopy," *Science* **321**, 379–382 (2008).
8. P. Thibault, M. Dierolf, O. Bunk, A. Menzel, and F. Pfeiffer, "Probe retrieval in ptychographic coherent diffractive imaging," *Ultramicroscopy* **109**, 338–343 (2009).
9. M. Guizar-Sicairos and J. R. Fienup, "Measurement of coherent x-ray focused beams by phase retrieval with transverse translation diversity," *Opt. Express* **17**, 2670–2685 (2009).
10. C. M. Kewish, M. Guizar-Sicairos, C. Liu, J. Qian, B. Shi, C. Benson, A. M. Khounsary, J. Vila-Comamala, O. Bunk, J. R. Fienup, A. T. Macrander, and L. Assoufid, "Reconstruction of an astigmatic hard x-ray beam and alignment of K-B mirrors from ptychographic coherent diffraction data," *Opt. Express* **18**, 23420–23427 (2010).
11. A. Schropp, P. Boye, J. M. Feldkamp, R. Hoppe, J. Patommel, D. Samberg, S. Stephan, K. Giewekemeyer, R. N. Wilke, T. Salditt, J. Gulden, A. P. Mancuso, I. A. Vartanyants, E. Weckert, S. Schder, M. Burghammer, and C. G. Schroer, "Hard x-ray nanobeam characterization by coherent diffraction microscopy," *Appl. Phys. Lett.* **96**, 091102 (2010).

12. J. Vila-Comamala, A. Diaz, M. Guizar-Sicairos, A. Mantion, C. M. Kewish, A. Menzel, O. Bunk, and C. David, "Characterization of high-resolution diffractive x-ray optics by ptychographic coherent diffractive imaging," *Opt. Express* **19**, 21333–21344 (2011).
13. A. Schropp, R. Hoppe, J. Patommel, D. Samberg, F. Seiboth, S. Stephan, G. Wellenreuther, G. Falkenberg, and C. Schroer, "Hard x-ray scanning microscopy with coherent radiation: Beyond the resolution of conventional x-ray microscopes," *Appl. Phys. Lett.* **100**, 253112 (2012).
14. Y. Takahashi, A. Suzuki, N. Zetsu, Y. Kohmura, Y. Senba, H. Ohashi, K. Yamauchi, and T. Ishikawa, "Towards high-resolution ptychographic x-ray diffraction microscopy," *Phys. Rev. B* **83**, 214109 (2011).
15. Y. Takahashi, A. Suzuki, S. Furutaku, K. Yamauchi, Y. Kohmura, and T. Ishikawa, "High-resolution and high-sensitivity phase-contrast imaging by focused hard X-ray ptychography with a spatial filter," *Appl. Phys. Lett.* **102**, 094102 (2013).
16. R. N. Wilke, M. Vassholz, and T. Salditt, "Semi-transparent central stop in high-resolution X-ray ptychography using Kirkpatrick–Baez focusing," *Acta Cryst. A* **69**, 490–497 (2013).
17. A. M. Maiden, M. J. Humphry, F. Zhang, and J. M. Rodenburg, "Superresolution imaging via ptychography," *J. Opt. Soc. Am. A* **28**, 604–612 (2011).
18. P. Thibault and A. Menzel, "Reconstructing state mixtures from diffraction measurements," *Nature* **494**, 68–71 (2013).
19. A. Maiden, G. Morrison, B. Kaulich, A. Gianoncelli, and J. Rodenburg, "Soft X-ray spectromicroscopy using ptychography with randomly phased illumination," *Nat. Commun.* **4**, 1669 (2013).
20. A. M. Maiden, M. J. Humphry, and J. M. Rodenburg, "Ptychographic transmission microscopy in three dimensions using a multi-slice approach," *J. Opt. Soc. Am. A* **29**, 1606–1614 (2012).
21. M. Dierolf, A. Menzel, P. Thibault, P. Schneider, C. M. Kewish, R. Wepf, O. Bunk, and F. Pfeiffer, "Ptychographic X-ray computed tomography at the nanoscale," *Nature* **467**, 436–439 (2010).
22. A. Diaz, P. Trtik, M. Guizar-Sicairos, A. Menzel, P. Thibault, and O. Bunk, "Quantitative X-ray phase nanotomography," *Phys. Rev. B* **85**, 020104(R) (2012).
23. M. Holler, J. Raabe, A. Diaz, M. Guizar-Sicairos, C. Quitmann, A. Menzel, and O. Bunk, "An instrument for 3D X-ray nano-imaging," *Rev. Sci. Instrum.* **83**, 073703 (2012).
24. M. Holler, A. Diaz, M. Guizar-Sicairos, P. Karvinen, E. Färm, E. Härkönen, M. Ritala, A. Menzel, J. Raabe, and O. Bunk, "Hard x-ray ptychographic computed tomography at 16 nm 3D resolution," *Sci. Rep.* **4**, 3857 (2014).
25. M. Guizar-Sicairos, A. Diaz, M. Holler, M. S. Lucas, A. Menzel, R. A. Wepf, and O. Bunk, "Phase tomography from X-ray coherent diffractive imaging projections," *Opt. Express* **19**, 21345–21357 (2011).
26. R. N. Wilke, M. Priebe, M. Bartels, K. Giewekemeyer, A. Diaz, P. Karvinen, and T. Salditt, "Hard x-ray imaging of bacterial cells: nano-diffraction and ptychographic reconstruction," *Opt. Express* **20**, 19232–19254 (2012).
27. M. W. M. Jones, G. A. van Riessen, B. Abbey, C. T. Putkunz, M. D. Junker, E. Balaur, D. J. Vine, I. McNulty, B. Chen, B. D. Arhatari, S. Frankland, K. A. Nugent, L. Tilley, and A. G. Peele, "Whole-cell phase contrast imaging at the nanoscale using Fresnel coherent diffractive imaging tomography," *Sci. Rep.* **3**, 2288 (2013).
28. P. Trtik, A. Diaz, M. Guizar-Sicairos, A. Menzel, and O. Bunk, "Density mapping of hardened cement paste using ptychographic X-ray computed tomography," *Cem. Concr. Compos.* **36**, 71–77 (2013).
29. B. Chen, M. Guizar-Sicairos, G. Xiong, L. Shemilt, A. Diaz, J. Nutter, N. Burdet, S. Huo, J. Mancuso, A. Monteith, F. Vergeer, A. Burgess, and I. Robinson, "Three-dimensional structure analysis and percolation properties of a barrier marine coating," *Sci. Rep.* **3**, 1177 (2013).
30. A. Diaz, M. Guizar-Sicairos, A. Poeppel, A. Menzel, and O. Bunk, "Characterization of carbon fibers using X-ray phase nanotomography," *Carbon* **67**, 98–103 (2014).
31. M. Esmacili, J. B. Fløystad, A. Diaz, K. Høydalsvik, M. Guizar-Sicairos, J. W. Andreasen, and D. W. Breiby, "Ptychographic X-ray tomography of silk fiber hydration," *Macromolecules* **46**, 434–439 (2013).
32. R. Dinapoli, A. Bergamaschi, B. Henrich, R. Horisberger, I. Johnson, A. Mozzanica, E. Schmid, B. Schmitt, A. Schreiber, X. Shi, and G. Theidel, "Eiger: Next generation single photon counting detector for x-ray applications," *Nucl. Instr. Meth. Phys. Res. A* **650**, 79–83 (2011).
33. I. Johnson, A. Bergamaschi, J. Buitenhuis, R. Dinapoli, D. Greiffenberg, B. Henrich, T. Ikonen, G. Meier, A. Menzel, A. Mozzanica, V. Radicci, D. K. Satapathy, B. Schmitt, and X. Shi, "Capturing dynamics with Eiger, a fast-framing X-ray detector," *J. Synchrotron Radiat.* **19**, 1001–1005 (2012).
34. M. Dierolf, I. Zanette, B. Enders, P. Thibault, A. Menzel, O. Bunk, and F. Pfeiffer, "Ptychographic reconstructions using shared data sets," (presented in Coherence 2012, International Workshop on Phase retrieval and Coherent Scattering, Fukuoka, Japan, 18–21 June 2012).
35. M. Dierolf, A. Menzel, O. Bunk, F. Pfeiffer, and P. Thibault, "Ptychographic reconstructions using shared data sets," In preparation (2014).
36. B. Henrich, A. Bergamaschi, C. Broennimann, R. Dinapoli, E. F. Eikenberry, I. Johnson, M. Kobas, P. Kraft, A. Mozzanica, and B. Schmitt, "Pilatus: A single photon counting pixel detector for x-ray applications," *Nucl. Instrum. Methods Phys. Res. A* **607**, 247–249 (2009).
37. C. Ponchut, J. M. Rigal, J. Clément, E. Papillon, A. Homs, and S. Petitdemange, "MAXIPIX, a fast readout photon-counting x-ray area detector for synchrotron applications," *J. Instrum.* **6**, C01069 (2011).
38. R. A. Dilanian, G. J. Williams, L. W. Whitehead, D. J. Vine, A. G. Peele, E. Balaur, I. McNulty, H. M. Quiney,

- and K. A. Nugent, "Coherent diffractive imaging: a new statistically regularized amplitude constraint," *New J. Phys.* **12**, 093042 (2010).
39. P. Thibault and M. Guizar-Sicairos, "Maximum-likelihood refinement for coherent diffractive imaging," *New J. Phys.* **14**, 063004 (2012).
 40. P. Kraft, A. Bergamaschi, C. Broennimann, R. Dinapoli, E. F. Eikenberry, B. Henrich, I. Johnson, A. Mozzanica, C. M. Schlepütz, P. R. Willmott, and B. Schmitt, "Performance of single-photon-counting PILATUS detector modules," *J. Synchrotron Radiat.* **16**, 368–375 (2009).
 41. T. B. Edo, D. J. Batey, A. M. Maiden, C. Rau, U. Wagner, Z. D. Pešić, T. A. Waigh, and J. M. Rodenburg, "Sampling in x-ray ptychography," *Phys. Rev. A* **87**, 053850 (2013).
 42. X. Llopart, M. Campbell, R. Dinapoli, D. San Segundo, and E. Pernigotti, "Medipix2: A 64-k pixel readout chip with 55 μm square elements working in single photon counting mode," *Nuclear Science, IEEE Transactions on* **49**, 2279–2283 (2002).
 43. R. Ballabriga, M. Campbell, E. Heijne, X. Llopart, L. Tlustos, and W. Wong, "Medipix3: A 64 k pixel detector readout chip working in single photon counting mode with improved spectrometric performance," *Nucl. Instrum. Methods Phys. Res. A* **633**(Supp. 1), S15–S18 (2011). 11th International Workshop on Radiation Imaging Detectors (IWORID).
 44. J. Marchal, I. Horswell, B. Willis, R. Plackett, E. N. Gimenez, J. Spiers, D. Ballard, P. Booker, J. A. Thompson, P. Gibbons, S. R. Burge, T. Nicholls, J. Lipp, and N. Tartoni, "EXCALIBUR: a small-pixel photon counting area detector for coherent X-ray diffraction - Front-end design, fabrication and characterisation," *J. Phys.: Conf. Ser.* **425**, 062003 (2013).
 45. A. Schropp, P. Boye, A. Goldschmidt, S. Hönig, R. Hoppe, J. Patommel, C. Rakete, D. Samberg, S. Stephan, S. Schöder, M. Burghammer, and C. G. Schroer, "Non-destructive and quantitative imaging of a nano-structured microchip by ptychographic hard X-ray scanning microscopy," *J. Microsc.* **241**, 9–12 (2011).
 46. P. Godard, A. M. Carbone, G. F. Mastropietro, G. Chen, L. Capello, A. Diaz, T. H. Metzger, and J. Stangl, "Three-dimensional high-resolution quantitative microscopy of extended crystals," *Nat. Commun.* **2**, 568 (2011).
 47. D. J. Vine, D. Pelliccia, C. Holzner, S. B. Baines, A. Berry, I. McNulty, S. Vogt, A. G. Peele, and K. A. Nugent, "Simultaneous x-ray fluorescence and ptychographic microscopy of cyclotella meneghiniana," *Opt. Express* **20**, 18287–18296 (2012).
 48. I. Johnson, A. Bergamaschi, H. Billich, S. Cartier, R. Dinapoli, D. Greiffenberg, M. Guizar-Sicairos, B. Henrich, A. Mozzanica, B. Schmitt, X. Shi, and G. Tinti, "Eiger: A single photon counting X-ray detector," *J. Instrum.* In press (2014).
 49. B. Abbey, G. J. Williams, M. A. Pfeifer, J. N. Clark, C. T. Putkunz, A. Torrance, I. McNulty, T. M. Levin, A. G. Peele, and K. A. Nugent, "Quantitative coherent diffractive imaging of an integrated circuit at a spatial resolution of 20 nm," *Appl. Phys. Lett.* **93**, 214101 (2008).
 50. An application programming interface (API) specification for parallel programming. <http://openmp.org/>
 51. M. Guizar-Sicairos, S. T. Thurman, and J. R. Fienup, "Efficient subpixel image registration algorithms," *Opt. Lett.* **33**, 156–158 (2008).
 52. E. Lima, A. Diaz, M. Guizar-Sicairos, S. Gorelick, P. Pernot, T. Schleier, and A. Menzel, "Cryo-scanning X-ray diffraction microscopy of frozen-hydrated yeast," *J. Microsc.* **249**, 1–7 (2013).
 53. M. van Heel and M. Schatz, "Fourier shell correlation threshold criteria," *J. Struct. Biol.* **151**, 250–262 (2005).
 54. J. Thieme, J. Sedlmair, S.-C. Gleber, J. Prietzel, J. Coates, K. Eusterhues, G. Abbt-Braun, and M. Salome, "X-ray spectromicroscopy in soil and environmental sciences," *J. Synchrotron Radiat.* **17**, 149–157 (2010).
 55. K. Medjoubi, N. Leclercq, F. Langlois, A. Buteau, S. Lé, S. Poirier, P. Mercère, M. C. Sforza, C. M. Kewish, and A. Somogyi, "Development of fast, simultaneous and multi-technique scanning hard X-ray microscopy at Synchrotron Soleil," *J. Synchrotron Radiat.* **20**, 293–299 (2013).
 56. S. T. Kelly, P. Nigge, S. Prakash, A. Laskin, B. Wang, T. Tyliczszak, S. R. Leone, and M. K. Gilles, "An environmental sample chamber for reliable scanning transmission x-ray microscopy measurements under water vapor," *Rev. Sci. Instrum.* **84**, 073708 (2013).
 57. M. Dierolf, P. Thibault, A. Menzel, C. M. Kewish, K. Jefimovs, I. Schlichting, K. von Knig, O. Bunk, and F. Pfeifer, "Ptychographic coherent diffractive imaging of weakly scattering specimens," *New J. Phys.* **12**, 035017 (2010).
 58. P. Braun, "On-the-fly scans for x-ray ptychography," Master's thesis, Université Montpellier 2 (2013).
 59. A. M. Maiden and J. M. Rodenburg, "An improved ptychographical phase retrieval algorithm for diffractive imaging," *Ultramicroscopy* **109**, 1256–1262 (2009).

1. Introduction

From its original demonstration [1] X-ray coherent diffractive imaging (CDI) keeps rising in interest as it offers unique imaging properties, such as an image contrast that is quantitatively interpretable as electron density and resolution that is not limited by lens manufacturing. For CDI in general highly spatially and temporally coherent illuminations are used, and an image of

the sample is obtained from the far-field intensity pattern through iterative reconstruction algorithms. The development of image reconstruction for CDI leans heavily on earlier developments for electron imaging [2] and robust phase retrieval algorithms initially applied to astronomical imaging [3]. Variants of CDI, such as Fresnel CDI [4] and ptychography [5], introduce modifications known *a priori* in the measurements in order to alleviate ambiguities and increase the robustness and reliability of the reconstructions.

For ptychography the sample is scanned through the beam with some degree of overlap, and a far-field diffraction pattern is measured at each point of the scan [5]. Such measurements have complementary information and the phase retrieval problem applied to all of them simultaneously yields significantly improved convergence speed and reliability of the reconstruction, where ambiguities are overcome due to transverse translational diversity in the measured data [6]. Refinement or retrieval of the illumination function [6–8] makes ptychography also suitable for characterization of coherent X-ray focused wavefronts [9–12]

An advantage gained through scanning in ptychography is that it allows for imaging extended regions of non-isolated samples with a customizable field of view (FOV). X-ray ptychography with a 2D resolution of around 10 nm, well below the size of the beam and the scanning steps, has been demonstrated [12–16], and significant developments continue to emerge where ptychography is, for instance, used for super-resolution [17], to recover coherent modes on the object or illumination [18], the spectral response of the specimen [19], or 3D sectioning from 2D scans [20]. Ptychography also finds valuable applications for 3D X-ray imaging. Originally demonstrated on a mouse femur section [21], ptychographic nanotomography delivers a unique combination of quantitative electron density contrast [22] and high 3D resolution [23, 24], and finds applications for biological specimens [25–27], materials science samples [28–30] and *in-situ* studies under variable environmental conditions [31].

A key criterion for the applicability and wide-spread use of ptychography as an X-ray microscopy tool is the achievable imaging rate. In this manuscript we demonstrate for ptychography an imaging rate above 25,000 resolution elements per second using Eiger, a next-generation photon-counting detector [32, 33]. Additionally we present an application of shared information between ptychography data sets [34, 35], that allows for measuring regions beyond the range of the piezoelectric positioning systems while simultaneously avoiding artifacts due to long term changes in the illumination function during the scan.

2. Diffraction intensity sampling

The X-ray measurement requirements for ptychography data sets are stringent. On a typical scan hundreds of far-field diffraction patterns are to be measured with a high dynamic range, negligible point spread function, and high signal-to-noise ratio (SNR). Instrumental to the success and practical application of ptychography has been the use of fast-readout photon-counting pixel detectors that allow such measurements in a reasonable time, without the need to stitch measurements with different attenuation, and with noise limited only by Poisson statistics [36, 37]. In particular, knowledge of such well defined noise statistics can be incorporated into the reconstruction algorithms [38, 39] which significantly improves image quality.

Compared to its predecessor, *i.e.* the Pilatus [36, 40] with a pixel size of 172 μm , the smaller pixel size of the Eiger detector of 75 $\mu\text{m} \times 75 \mu\text{m}$ allows to sample finer coherent speckle while preserving single-photon counting with zero readout noise, high dynamic range, frame rate capability up to 22 kHz, and a negligible deadtime between frames of 4 μs [32]. To avoid aliasing and loss of information in the measurement the far-field intensity should be at least Nyquist sampled, which imposes a limit in the maximum transverse extent of the X-ray illumination, w , to

$$w = \frac{\lambda z}{2\Delta}, \quad (1)$$

where λ is the X-ray wavelength, z is the distance from the sample to the detector, and Δ is the detector pixel size. Hence, given a fixed sample-detector distance the smaller pixel of the Eiger directly enables the use of an X-ray illumination that is larger in the transverse direction, which allows for a coarser scanning step and significantly reduces the overhead of ptychography scans due to sample positioning. While it has been shown that sampling of the speckle pattern may be significantly relaxed in the case of ptychography, the scaling of the scan step size still applies in order to acquire a well-behaved data set [41], *i.e.*, the detector pixel size still directly influences the scanning time overhead.

An advantage of Eiger in comparison to many other detector systems is the large number of pixels within a single module and the comparatively small area between detector modules of large area systems. Photon counting X-ray detectors based on Medipix2 [42] and Medipix3 [43] technology, such as Maxipix [37] and Excalibur [44], should give similar performance given their fast readout and small pixel size of 55 μm . While such detectors are used successfully for ptychography [11, 16, 41, 45–47], the acquisition rates reported thus far are slower by more than an order of magnitude than the one presented here, presumably due to a focus toward demonstrating other capabilities such as concomitant fluorescence imaging or high resolution. At the same time, experimental conditions as shown here probe the limits of systems such as Maxipix [37], and for the application of ptychography in next-generation high-brilliance sources and considering the continuous improvement in X-ray optics efficiency, even the higher count rate capabilities and dynamic range of Eiger [32] will be pushed to their limits.

The X-ray measurements shown here were carried out at the cSAXS beamline, Swiss Light Source, Paul Scherrer Institut, Switzerland, using a single-module Eiger detector with 512×1024 pixels that has been recently installed and commissioned [48].

3. Experiment

The incident radiation on the sample had a photon energy of 6.2 keV ($\lambda = 0.2$ nm) defined by a Si(111) double crystal monochromator. The illumination was focused by a gold Fresnel zone plate (FZP) with 100 μm diameter, 100 nm outermost zone width, and approximately 1 μm zone height, which at this energy produces a focused beam at 50 mm from the lens. A combination of a 30 μm diameter central beamstop and 20 μm order-sorting aperture (OSA), as shown in Fig. 1(a), blocks the undiffracted beam and higher diffraction orders from the FZP.

In order to study a known object with contrast and features representative of a real application we used an Eiger detector readout chip as a sample. To increase X-ray transmission the backside silicon was etched by inductively-coupled plasma reactive-ion etching to a final thickness of about 10 μm . Integrated circuits have been used in the past as test samples to demonstrate high-resolution quantitative imaging of buried structures by Fresnel CDI and ptychography [23, 45, 49]. The sample was mounted on a 2D piezoelectric translation stage (Physik Instrumente P-733.2CL) that allows for nanometric movements transverse to the direction of X-ray propagation and a total travel range of 100 $\mu\text{m} \times 100 \mu\text{m}$. This stage was in turn mounted on a coarse stepper motor translation stage to allow for imaging beyond the scanning range of the piezoelectric stage. The sample was located 5 mm downstream of the focus. At this distance the diameter of the X-ray illumination is approximately 10 μm which is the maximum diameter that allows Nyquist sampling of the intensity patterns with the Eiger detector at 7.2 m from the sample and 6.2 keV photon energy, Eq. (1). Figures 1(b) and 1(c) show two example diffraction patterns.

To avoid a reconstruction ambiguity arising from periodic scanning grids [8] ptychography scans were performed in a pattern of concentric circles with FOV of 80 $\mu\text{m} \times 80 \mu\text{m}$, where the n -th circular shell has $5n$ points, 3.5 μm radial spacing, 0.2 second exposure time, and an average count of 9.5×10^6 photons per diffraction pattern. These scans resulted in 423 points

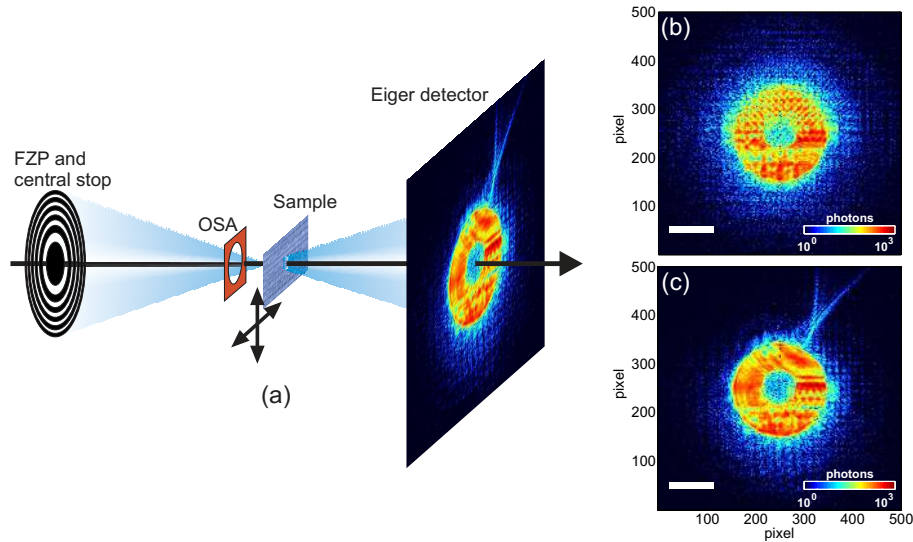


Fig. 1. (a) Experimental setup. The sample is mounted on a scanning system and is illuminated by a $10\ \mu\text{m}$ beam focused by an X-ray FZP. (b) and (c) show example diffraction patterns from a ptychography scan in logarithmic scale with 0.2 second exposure time, scale bars correspond to $30\ \text{radians}/\mu\text{m}$

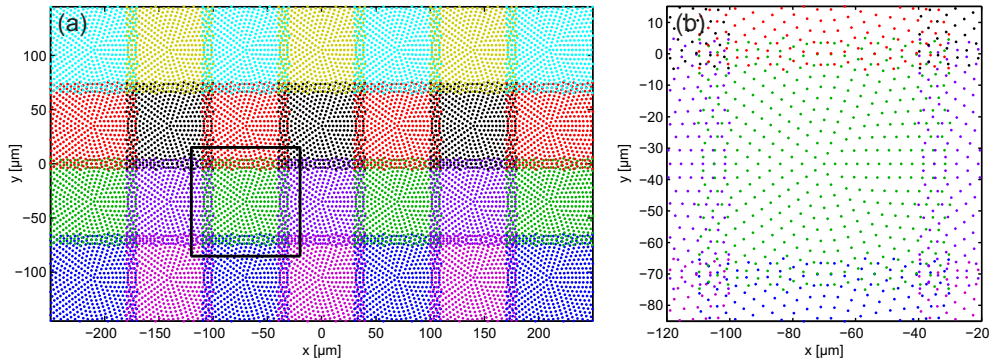


Fig. 2. (a) Scanning points for a $500\ \mu\text{m} \times 290\ \mu\text{m}$ FOV. Ptychography scans of $80\ \mu\text{m} \times 80\ \mu\text{m}$ are repeated after $70\ \mu\text{m}$ translation using coarse stages, having $10\ \mu\text{m}$ overlap between scans. The solid square denotes the inset area shown in (b).

and took 151 seconds each. The scan overhead of 0.15 seconds per point was primarily due to the settling time of the piezoelectric positioning system. For comparison, a scan of similar quality, with the same total exposure time and FOV would require $1.3\ \mu\text{m}$ radial spacing and 3000 scanning points with the Pilatus detector and would take approximately 540 seconds.

A larger region was measured by using the coarse translations to shift the sample and piezoelectric stage to different positions in a 7×4 rectangular mesh with $70\ \mu\text{m}$ spacing. At each point of this mesh the ptychography scan of $80\ \mu\text{m} \times 80\ \mu\text{m}$ FOV was repeated as shown in Fig. 2. The overlap region between scans is important in order to reconstruct the whole measurement as a single data set. The full measurement of a $500\ \mu\text{m} \times 290\ \mu\text{m}$ region was carried out in 70 minutes.

4. Reconstruction-the Eiger self-portrait

From the measured diffraction patterns a 500×500 pixel region of the detector centered on the FZP illumination cone was extracted for further processing, resulting in a reconstruction pixel size of 38.4 nm. All reconstructions described in this manuscript were performed with a hybrid message passing interface (MPI) and OpenMP [50] code, currently under development at the Scientific Computing Group of the Paul Scherrer Institut, Switzerland, using 400 iterations of the difference map algorithm [7] followed by 200 iterations of maximum likelihood optimization as a refinement step [39]. Initially the individual ptychography scans were reconstructed independently using as initial guess for the X-ray illumination an ideal focused beam numerically propagated 5 mm downstream of the focus. From these reconstructions we identified and characterized a systematic positioning error in the scanning stages attributed to the yaw angular error of the piezoelectric system which was later confirmed and characterized using an autocollimator (Elcomat, Möller-Wedel Optical GmbH, Germany). After applying a suitable affine transformation the corrected scanning position coordinates were fed into the reconstruction algorithm and resulted in improved image quality and sharpness and decreased noise in the reconstruction.

The coarse translation stages used for increasing the measurement FOV are also a source of positioning error. The nominal positions of the coarse stage positions provided an initial estimate of the relative translations between the reconstructions from individual ptychography scans, and from these the overlapping regions between reconstructions were determined. Positioning errors between scans were obtained using an efficient crosscorrelation-based subpixel image registration algorithm [51]. After this initial registration step we obtain a more accurate estimate of the overlap region between different scans, and using this improved overlap estimate to compute a new crosscorrelation image registration gives in turn a more accurate result. We applied this process iteratively until the registration values converged, which occurs typically in about 10 iterations, providing in the end an accurate subpixel correction for the positioning errors of the coarse stages.

Another limitation for long ptychography measurements is the stability of the illuminating probe throughout the duration of the full scan, since the reconstruction algorithm attempts to find a complex-valued object and a time-invariant illumination that reproduces the measured diffraction patterns. For cases where the illumination suffers from significant changes during a scan the reconstruction can exhibit artifacts. This problem was addressed by sharing information between different scans, an approach that was originally introduced to overcome probe instabilities for acquiring statistics on weakly scattering samples [34, 35]. Information sharing between data sets is superior to averaging of images [52] and has further proven useful for dealing with unconstrained intensities due to detector gaps in high-resolution ptychography [12, 24, 34, 35]. Here we apply this concept by reconstructing a single object while keeping a different reconstructed probe per scan. During the reconstruction we take advantage of the increased statistics in regions where scans overlap, and inherent degrees of freedom such as constant and linear phase offsets between different individual scans [25] are also automatically matched during the iteration procedure. A detailed discussion and results specific to information sharing and its application to ameliorate artifacts, deal with detector gaps and acquire statistics on radiation-sensitive specimens will be the focus of an upcoming publication [35], here for completeness we provide details of our implementation in Appendix A.

The positioning errors between scans, obtained by subpixel image registration, were accounted for in the ptychography reconstruction by suitable transverse shifting of the corresponding 28 initial probe estimates. At each iteration a single complex-valued 98.4 megapixel object ($13,028 \times 7,556$) is updated using all 11,844 diffraction patterns, meanwhile 28 probe illumination functions of 500×500 pixels are updated from the 423 diffraction patterns of the

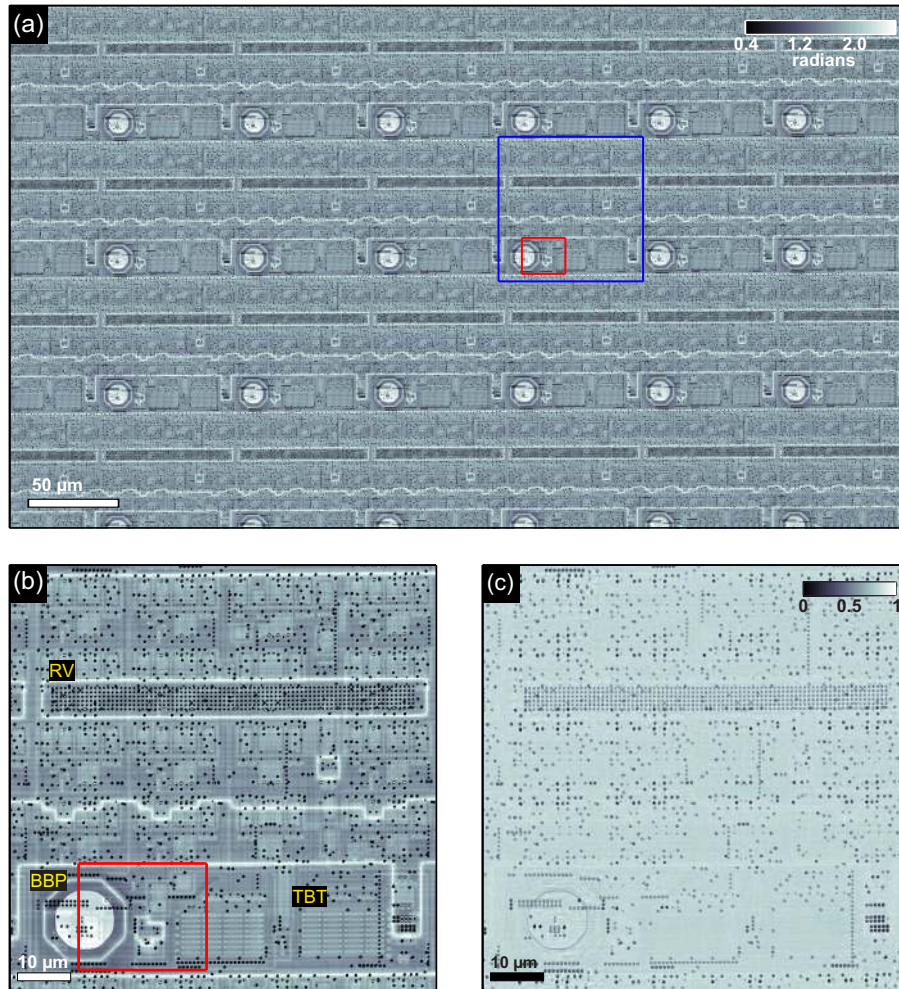


Fig. 3. (a) Phase of $500\ \mu\text{m} \times 290\ \mu\text{m}$ reconstruction of the sample, an Eiger readout chip, imaged with 98.4 megapixels. Although the phase of the reconstruction covers the range of $[-\pi, \pi]$ radians, for better visualization of low-contrast details a range of $[0.4, 2.6]$ radians is shown. (b) Inset of $80\ \mu\text{m} \times 80\ \mu\text{m}$, indicated by a blue rectangle in (a) and with the same color scale, shows a full Eiger pixel. Labeled are rows of tungsten vias (RV), the pixel bump bond pad (BBP) and an array of 64 trim-bit linear transistors (TBT). Red rectangles in (a) and (b) outline the $24\ \mu\text{m} \times 20\ \mu\text{m}$ inset shown in Fig. 4(a) and Fig. 4(d). (c) Amplitude of the reconstruction inset shown in (b).

corresponding scan. The final reconstruction was carried out in 90 minutes with 12 compute nodes on the Merlin HPC cluster at PSI. The nodes are HP G8 Blades with 64 GB memory and two 2.6 GHz 8 core Intel SandyBridge CPUs each, interconnected with QDR Mellanox ConnectX 3 Infiniband.

Figure 3(a) shows the phase of the reconstruction of the $500\ \mu\text{m} \times 290\ \mu\text{m}$ FOV, where dark colors indicate more negative phase values, which correspond to higher electron density or traversing more material. Figure 3(b) shows an $80\ \mu\text{m} \times 80\ \mu\text{m}$ inset that displays a full pixel of the Eiger readout chip. Multiple tungsten vias that connect two or more chip layers, in particular arranged rows of these vias (RV), appear as high-contrast round dark circles of ap-

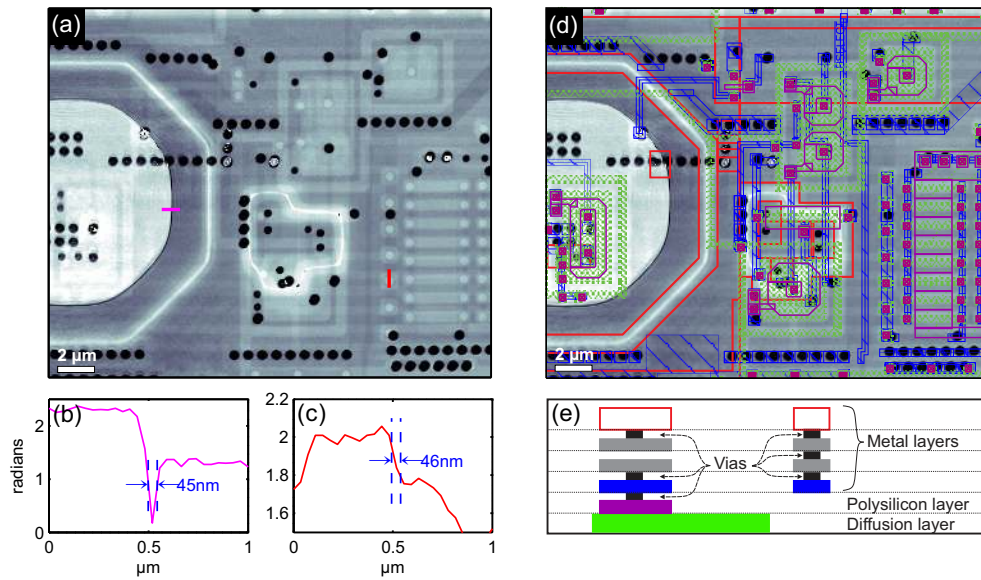


Fig. 4. (a) Inset of $24\ \mu\text{m} \times 20\ \mu\text{m}$ of the reconstruction, denoted by red rectangles in Figs. 3(a) and 3(b) and shown with the same phase range. The detail of tungsten vias connections between layers, which appear as dark circles, and the BBP and transistor elements can be better inspected. Line profiles, indicated in (a) by solid lines, show (b) a resolved line feature with 45 nm full-width-half-maximum and (c) an edge response (10% - 90%) of 46 nm. (d) Image in (a) with an overlay of some layers of the chip design. The borders of the top metal layer are shown in red. As expected these borders surround the lines of gaps that appear in the X-ray image in white. The two components of linear and round transistors, the polycrystalline silicon and diffusion layers, are shown in purple and green, respectively. A layer of metal interconnects is shown in blue. (e) Schematic of the layered structure of the Eiger readout chip. Intermediate metal layers shown in gray here are not shown in (d) for clarity.

proximately 400 nm diameter. The pixel bump bond pad (BBP) is seen enclosed in an octagonal gap (white line) and with a central circular passivation opening that appears light colored. In the reconstruction one can resolve all transistors in the chip design with fine detail, for instance the labeled array of 64 linear trim-bit transistors (TBT). Figure 4(a) shows an even smaller inset of $24\ \mu\text{m} \times 20\ \mu\text{m}$ where the quality of the reconstruction and level of detail can be better appreciated for the tungsten vias, the BBP, and multiple transistor components such as elements of the TBT. In Fig. 4(d) we overlay layers of the chip design on the reconstruction in order to correlate expected and observed features. In red we emphasize edges of the topmost aluminium layer, the gaps of this layer appear in the reconstruction as white lines as the X-rays traverse less material at those positions. The polycrystalline silicon and diffusion layers, which are the building blocks of transistor gates, are shown in purple and green respectively. During etching of the backside silicon these two layers were selectively removed, hence an otherwise very low contrast is here emphasized due to the resulting relief structure in the backside of the chip. Additionally multiple buried line connectors in other metal layers can be seen in Fig. 4(a), but for clarity only one of them is overlaid in Fig. 4(d) in blue.

For resolution estimation the first scan of the series, with $80\ \mu\text{m} \times 80\ \mu\text{m}$ FOV, was measured twice. The two independent reconstructions were then aligned to a small fraction of a

pixel [51] and the resolution of one of these images was estimated to 41 nm by comparing their Fourier shell correlation (FSC) curve with the 1-bit threshold curve [12, 53]. This estimate was confirmed by line profiles of a sharp line and an edge response, shown in Figs. 4(b) and 4(c), respectively. In the latter an edge response of 46 nm was obtained on a relatively low-contrast feature of about 0.2 radians. For a single ptychography scan we have then 3.8×10^6 resolution elements (1951×1951). Based on the FSC curve and the fact that the noise, sharpness and level of detail is preserved across the larger reconstruction we conclude that this resolution is preserved throughout the entire measurement, hence resulting in a total of 86.2×10^6 resolution elements ($12,195 \times 7,073$) for the full 98.4 megapixel object reconstruction.

5. Discussion

Here we present the first ptychography reconstruction using Eiger, a new-generation photon-counting detector, and demonstrate the increased imaging rate capabilities this detector allows for ptychography due to the Poisson limited noise, single-pixel point spread function, high dynamic range, fast readout, and small pixel size. Reconstructions from individual scans with $80 \mu\text{m} \times 80 \mu\text{m}$ were obtained with a 38.4 nm pixel size and 41 nm resolution. These individual images have 3.8×10^6 resolution elements and were acquired in 151 seconds, which demonstrates an imaging rate of 25.2×10^3 resolution elements per second or an effective dwell time of 40 μs per resolution element, a rate that is state-of-the-art for CDI, ptychography, and competitive with scanning transmission X-ray microscopy end stations for which dwell times per point on fast instruments are hardware limited to 50 μs but with measurement times typically around 1 ms per resolution element [54–56].

We demonstrate fast imaging rate on large regions and extended periods of time by imaging a $500 \mu\text{m} \times 290 \mu\text{m}$ region of an Eiger integrated chip with 41 nm resolution and 86.2×10^6 resolution elements, measured in 70 minutes. To avoid artifacts due to probe changes during the whole acquisition, for the reconstruction we apply information sharing between individually fast scans which allows a single object and multiple illuminations to be reconstructed. The imaging rate for this case was reduced to 20.5×10^3 resolution elements per second because the effective individual scan area is slightly reduced due to the overlap between adjacent ptychography scans.

As for any imaging technique, the performance of ptychography given here may vary depending on the sample contrast and desired resolution, *i.e.* longer scanning times are needed to acquire statistics and obtain high-resolution images on low-contrast specimens, such as unstained biological samples [26, 52, 57]. However this increase in needed statistics is in part compensated by the use of ptychography at new-generation high-brightness sources, further improvements in efficiency of optics for collecting coherent flux, and reduction of positioning overhead, provided that development of adequate detector technology continues. In particular, note that the overhead of 0.15 seconds per point in our measurement already constitutes around 43% of the measurement time. With advance of faster scanning stages or development of reconstructions from on-the-fly scans [58] there is potential for an increase in imaging rate beyond 44×10^3 resolution elements per second already with the photon flux of the current experiment.

Appendix A. implementation of information sharing between data sets

In ptychography the interaction between the sample and the incident X-ray illumination is typically represented through the product of 2D complex-valued arrays that correspond to the incident X-ray wavefield or probe, $P(\mathbf{r})$, and the transmissivity of the object, $O(\mathbf{r})$. The exit wavefield, also referred to as view, for the j -th scanning position, \mathbf{r}_j , is given by

$$\psi_j(\mathbf{r}) = P(\mathbf{r} - \mathbf{r}_j)O(\mathbf{r}), \quad (2)$$

where $\mathbf{r} = (x, y)$ represents the Cartesian coordinates transverse to the beam propagation direction. The measurements are typically taken in the far-field such that the intensity of the Fourier transform of the exit fields is measured,

$$I_j(\mathbf{q}) = |\mathcal{F}\{\psi_j(\mathbf{r})\}|^2, \quad (3)$$

where $\mathcal{F}\{\cdot\}$ represents a Fourier transform and \mathbf{q} are the reciprocal space coordinates. The goal of the reconstruction algorithm is to find $O(\mathbf{r})$ and $P(\mathbf{r})$ that agree with the measured intensities, $I_j(\mathbf{q})$, for all scanning points.

The problem can be generalized to allow for multiple data sets to be reconstructed jointly, by allowing M different objects and N probes in the reconstruction procedure. Here by joint reconstruction we mean that the reconstruction of these separate data sets will be coupled to each other during the iteration procedure through a common probe or object. The choice of which function is common between data sets varies depending on the specific experimental scenario, for instance, to deal with detector gaps for tomography two data sets and two different objects are coupled through a common probe [24, 35].

The exit wavefield is the product of one probe and one object out of a set of M objects and N probes. Then in general

$$\psi_j(\mathbf{r}) = P_{n_j}(\mathbf{r} - \mathbf{r}_j) O_{m_j}(\mathbf{r}), \quad (4)$$

where $m_j \in [1, \dots, M]$ and $n_j \in [1, \dots, N]$. The object m_j and illumination n_j are then associated to the intensity measurement j and conventional ptychography is recovered by assigning all indices to one object and one illumination, i.e. $\forall j: (m_j = 1, n_j = 1)$.

For the application of this sharing scheme to extending the FOV, as described in the main manuscript, the reconstruction was of a single complex-valued object, $M = 1$, but allowing for multiple illuminations, $N = 28$. Although in general it is not required, in our case all scans had the same number of points. The probe indices are then

$$n_j = \begin{cases} 1, & \text{if } 1 \leq j \leq 423 \\ 2, & \text{if } 424 \leq j \leq 846 \\ \vdots & \\ k, & \text{if } 1 + (k-1)423 \leq j \leq 423k \end{cases} \quad (5)$$

which relaxes the illumination stability requirements since the illumination is assumed constant only within a set of 423 points taken in 150 seconds. Furthermore, by requiring a single object, the reconstruction profits from increased statistics in the overlap regions between scans. Constant and linear phase offsets, which are inherent ambiguities of ptychography [25], are automatically matched through the unique object reconstruction.

For iterative transform algorithms, such as the difference map [8] and extended ptychographic iterative engine (ePIE) [59], the application of the Fourier domain constraint remains unchanged, and the main modification to the algorithm is during the update of the object and probe. For the particular case of the difference map, the overlap projection [8] now requires the solution of the modified coupled equations

$$O_k(\mathbf{r}) = \frac{\sum_{j=\{j'|m_{j'}=k\}} P_{n_j}^*(\mathbf{r} - \mathbf{r}_j) \psi_j(\mathbf{r})}{\sum_{j=\{j'|m_{j'}=k\}} |P_{n_j}(\mathbf{r} - \mathbf{r}_j)|^2}, \quad (6a)$$

$$P_l(\mathbf{r}) = \frac{\sum_{j=\{j'|n_{j'}=l\}} O_{m_j}^*(\mathbf{r} + \mathbf{r}_j) \psi_j(\mathbf{r} + \mathbf{r}_j)}{\sum_{j=\{j'|n_{j'}=l\}} |O_{m_j}(\mathbf{r} + \mathbf{r}_j)|^2}, \quad (6b)$$

for $k = [1, \dots, M]$ and $l = [1, \dots, N]$ and where $*$ denotes complex conjugate. Notice that the sum index j runs only over the diffraction patterns that are associated with the left-hand side object or probe. On the right-hand side, the update is carried out using the object or probe associated to the j -th diffraction pattern. A similar generalization can be applied to the ePIE algorithm update step to allow several objects and probes.

For maximum likelihood optimization, the negative log-likelihood given the observed measurements, \mathcal{L} , is used as the error metric to be minimized through gradient-based non-linear optimization [6, 39]. Following the notation in [39] the expression for the computation of \mathcal{L} remains the same, as it is based on a comparison of the measured intensities with the Fourier transform of the exit wavefields, with the exception that these exit wavefields are now given by Eq. (4). The algorithm in this case is generalized by solving for several objects and illuminations using the gradient of the error metric with respect to all $O_{m_j}(\mathbf{r})$ and $P_{n_j}(\mathbf{r})$. The gradients of all objects and probes are then given by

$$g_{O_k}(\mathbf{r}) = \sum_{j=\{j' | m_{j'}=k\}} P_{n_j}(\mathbf{r} - \mathbf{r}_j) \chi_j^*(\mathbf{r}), \quad (7a)$$

$$g_{P_l}(\mathbf{r}) = \sum_{j=\{j' | n_{j'}=l\}} O_{m_j}(\mathbf{r} + \mathbf{r}_j) \chi_j^*(\mathbf{r} + \mathbf{r}_j), \quad (7b)$$

where

$$\tilde{\chi}_j(\mathbf{q}) = \frac{\partial \mathcal{L}}{\partial I_j(\mathbf{q})} \mathcal{F} \{ \psi_j(\mathbf{r}) \}. \quad (8)$$

Acknowledgments

We thank Xavier Donath for excellent support at cSAXS, Ivan Rajković for help during the experiments, Martin Dierolf, Pierre Thibault, Konstantins Jefimovs, J. Friso van der Veen, Bernd Schmitt and Gemma Tinti for fruitful discussions and Heinrich R. Billich for his support for the computing infrastructure around the Eiger detector at cSAXS.